Journal of Electrochemical Science and Technology
Vol. 2, No. 1, 2011, 45-50
DOI:10.5229/JECST.2011.2.1.045

Journal of Electrochemical Science and Technology

Expanded Graphite Negative Electrode for Lithium-ion Batteries

Hyun D. Yoo[a], Ji Heon Ryu[b], Seongho Park[a], Yuwon Park[a], Bok H. Ka[a] and Seung M. Oh[a,†]

[a]*Department of Chemical and Biological Engineering and WCU program of C_2E_2, Seoul National University, 599 Gwanangno, Gwanak-gu, Seoul, 151-744, Korea*

[b]*Graduate School of Knowledge-based Technology and Energy, Korea Polytechnic University, 2121 Jeongwang-dong, Siheung-si, Gyeonggi-do 429-793, Korea*

ABSTRACT :

A series of expanded graphites is prepared from graphite oxide by changing the heat-treatment temperature, and their lithiation/de-lithiation mechanism and rate performance are examined. A featureless sloping profile is observed in their charge-discharge voltage and dilatometry profiles, which is contrasted by the stepwise plateau-like profiles observed with the pristine graphite. With an increase in the heat-treatment temperature from 250°C to 850°C, the interlayer distance becomes smaller whereas the electric conductivity becomes larger, both of which are resulted from a removal of foreign atoms (mainly oxygen) from the interlayer gaps. The expanded graphite that is prepared by a heat-treatment at 450°C delivers the best rate performance, which seems to be a trade-off between the Li^+ ion diffusivity that is affected by the interlayer distance and electrical conductivity.

Keywords : Lithium-ion batteries, Expanded graphites, Electrochemical dilatometry, Interlayer distance, Electrical conductivity

Received February 13, 2011 : Accepted March 9, 2011

1. Introduction

There have been intensive researches to develop negative electrode materials with high capacity, high rate capability, and longer cycle life. Until now, however, almost of the commercial lithium-ion batteries adopt the graphitic carbons as the negative electrode since these highly crystalline carbonaceous materials show a stable charge/discharge behavior at 0.0~0.3 V (*vs.* Li/Li^+). Indebted to such a low charge/discharge potential, 4 V lithium-ion cells have come into the market by combining with 4 V positive electrodes. Other advantages belonging to graphite electrodes are the relatively cheap price, long cycle life and low self-discharge rate. When considered as the power source for electric vehicles, however, they show some intrinsic limitations: capacity (theoretical value = 372 mAh g^{-1}) and poor rate capability. In particular, the graphite electrodes show a poor Li^+ intercalation kinetics, such that Li plating is frequently observed under high-rate charging condition.[1,2] Several approaches have been made to facilitate the Li^+ intercalation kinetics, which includes a modification of graphites, deliberate control of electrolytes, and introduction of non-graphitic carbons.[3-6]

The poor lithiation kinetics in graphite electrodes is inherited by the slow solid-state Li^+ diffusion into the graphene layers.[7,8] Therefore, an expansion of interlayer distance seems to be an appropriate approach to enhance the rate capability. To realize this in this work, an artificial graphite (MCMB, graphitized mesocarbon microbeads) is converted into a series of expanded graphites (*e*-MCMBs) having different interlayer distance.[9-11] Note that the term 'expanded' means an expansion of the microscopic interlayer, which is different to the exfoliated graphites that are macroscopically expanded with macro-pores.[12] The effects of interlayer distance and electrical conductivity on the rate performances of expanded graphites are examined, both of which are controlled by the heat-treatment temperature.

†Corresponding author. Tel.: +82-2-880-7074
E-mail address: seungoh@snu.ac.kr

2. Experimental

The graphite oxide (GO) was prepared by the modified Hummers method.[13,14] In detail, 5.0 g of MCMB_1028 (Osaka Gas Chemical Co., average particle size = 10 mm, graphitization temperature = 2800°C) was dispersed in a mixture of 95% sulfuric acid (60 mL) and 60% nitric acid (20 mL). Then, 10 g of potassium permanganate ($KMnO_4$, Aldrich) was slowly added as the oxidizing agent, while the reactants being ice-cooled. After stirring for one week at room temperature, the reaction mixture was poured into 2 L of water and stored for 12 h without stirring to obtain a carbon precipitate. The precipitate was poured into 2 L of water again and centrifugation/rinsing process was repeated until the pH of the floating water reaches ~7. Finally, the GO powder was collected after filtration and vacuum-drying at 60°C.

For the preparation of expanded graphites, the as-obtained GO powder was heat-treated at 250, 450, 650, and 850°C under argon atmosphere for 24 h. The heating ramp was controlled at 0.42°C min^{-1} to avoid the graphite exfoliation. The resulting expanded graphites were characterized by using a field-emission scanning electron microscope (FE-SEM, JEOL JSM-6700F), elemental analysis (EA1110, CE Instrument), Raman spectroscopy (Jobin Yvon, Lab Ram HR, λ = 514.5 nm), x-ray diffractometer (Rigaku, D-MAX2500-PC, Cu Kα, λ = 0.15405 nm) and nitrogen adsorption (Micromeritics, ASAP 2010). Electrical conductivity of the powder samples was measured by the van der Pauw method;[15] the powders were pressed into a thin film (~50 mm) in a homemade apparatus under the pressure of 2500 psi.

For the electrochemical tests, the composite electrodes were prepared by coating the slurry of active material, polyvinylidene fluoride (PVdF) binder, and conductive carbon (Super-P) (8 : 1 : 1 in wt. ratio in *N*-methyl-2-pyrrolidone solvent, 80 : 5 : 15 for dilatometry) on a piece of Cu foil (thickness = 10 μm). The electrode plates were roll-pressed to enhance the inter-particle contact and to ensure the adhesion to the current collector and then dried in vacuum oven at 120°C for 12 h. The loading amount of active mass in the electrodes was ~2.3 mg cm^{-2} and the thickness of the coated film was ~40 μm. The coin-type cells (CR2032) were assembled in a glove box with Li foil as the counter electrode, 1.0 *M* $LiPF_6$ in EC : DEC (1 : 1 in vol. ratio, where EC is ethylene carbonate and DEC is diethyl carbonate) as the electrolyte, and a porous polyethylene film as the separator. Galvanostatic charge-discharge cycling was made with a WBCS-3000 battery cycler (Wonatech Co.). The height change of the working electrodes was traced using a homemade electrochemical dilatometer;[16,17] the applied force was fixed at 3 N, which is given by the weight of the probe.

Cycle performance was tested by a constant current (CC) charge-discharge at 0.2C in the potential range of 0.01~2.5 V (*vs.* Li/Li^+) and a constant voltage (CV, at 10 mV) step was added in the lithiation period until the current drops to the half of charging current. For the rate tests, both the lithiation and de-lithiation rates were changed in the range of 0.5C~10C without the CV step. Before the rate test, the cells were preconditioned by cycling at 0.2C (with CV step at 10 mV *vs.* Li/Li^+) for two cycles. In this report, lithiation is expressed as discharging and de-lithiation as charging on the basis of the standard lithium-ion cell configuration.

3. Results and Discussion

3.1. Material characterizations

Fig. 1 shows the FE-SEM images obtained of the powders of MCMB_1028, graphite oxide (GO), and *e*-MCMBs. The spherical shape of MCMB_1028 is maintained in GO and *e*-MCMBs. Any particles with accordion-like shape are not found, implying that the

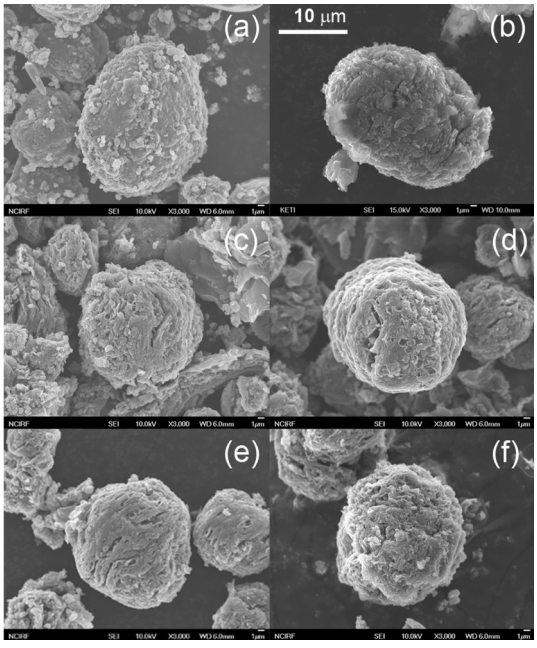

Fig. 1. FE-SEM images: (a) MCMB_1028, (b) graphite oxide, (c) *e*250, (d) *e*450, (e) *e*650, and (f) *e*850.

macroscopic graphite exfoliation is suppressed by the slow ramp (< 0.42°C min^{-1}) in the heating process. The BET (Brunauer-Emmett-Teller) surface area of *e*-MCMBs was 20~50 m^2 g^{-1}, which is larger than that for MCMB_1028 (2 m^2 g^{-1}) but still smaller than that for the exfoliated graphites. The average pore diameter was less than 5 nm, which is far smaller than that for the common exfoliated graphites. The apparent particle size of *e*-MCMBs is comparable to that of MCMB_1028 regardless of the heat-treatment temperature.

Fig. 2(a) displays the XRD patterns obtained of the powders of *e*-MCMBs and MCMB_1028. On the whole, the diffraction peaks are broader for *e*-MCMBs. The crystallite size along the *c*-axis (L_c) is calculated from the full-width at half-maximum values (*B*, measured on 2θ axis in radians) using Scherrer's equation, $L_c = 0.94\lambda/(B\cos\theta)$. The L_c values for *e*850 and MCMB_1028 are calculated to be ~5 nm and ~25 nm, respectively. The smaller L_c for *e*850 reflects that the graphene layers of MCMB_1028 are divided into many galleries of thinner layers by the strong oxidation and subsequent heat-treatment. The interlayer distance (d_{002}) is also calculated using Bragg's formula ($\lambda = 2d\sin\theta$) (Fig. 2(b)). The values for *e*-MCMBs are in the range of 0.40~0.338 nm, which is larger than that of MCMB_1028 (0.336 nm). In the series of expanded graphites, the d_{002} values decrease with an increase in the heat-treatment temperature, which must be due to the elimination of foreign atoms from the interlayer gaps. Namely, the foreign atoms (mainly oxygen) that are introduced during the GO preparation step are removed during the heat-treatment period. As listed in Table 1, the population of foreign atoms steadily decreases with an increase in the heat-treatment temperature.

Fig. 3 presents the electrical conductivity data obtained with *e*-MCMBs. The electrical conductivity increases with an increase in the heat-treatment temperature. It is known that MCMB_1028 is highly conductive (~200 S cm^{-1}), whereas GO is not (~0.02 S cm^{-1}) since the sp^2 bonds in graphene layers are transformed to sp^3 bonds by the introduction of foreign atoms. Hence, the conductivity increase with an increase in the heat-treatment temperature can be accounted for by the removal of foreign atoms. The

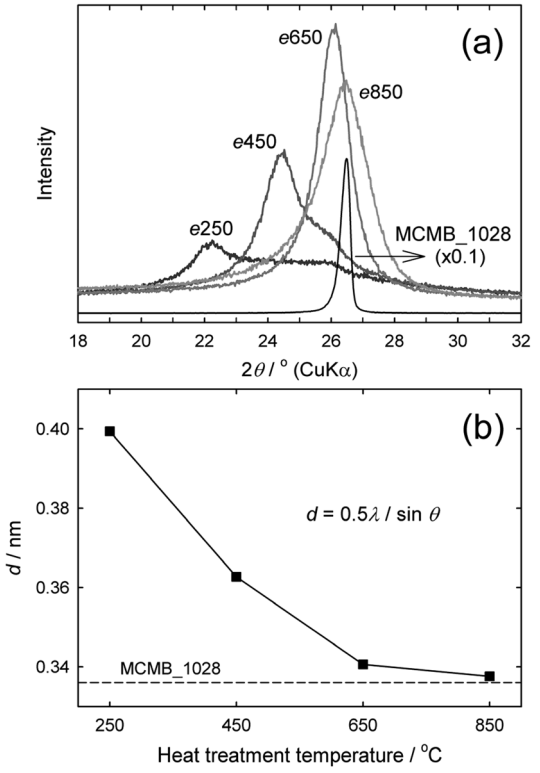

Fig. 2. (a) XRD patterns of the samples and (b) interlayer distance (d_{002}) of the *e*-MCMBs according to the heat-treatment temperature.

Table 1. Elemental analysis of the samples (wt. %)

	C	O	H	N	S	Ash content
MCMB_1028	99.1	0.1	0.0	-	-	0.8
GO	64.4	31.8	1.7	0.1	2.0	-
*e*250	79.9	14.6	0.4	0.1	0.8	4.2
*e*450	86.8	8.5	0.3	0.1	0.3	4.0
*e*650	91.1	4.5	0.3	0.1	0.4	3.6
*e*850	93.3	1.7	0.4	0.2	0.4	4.0

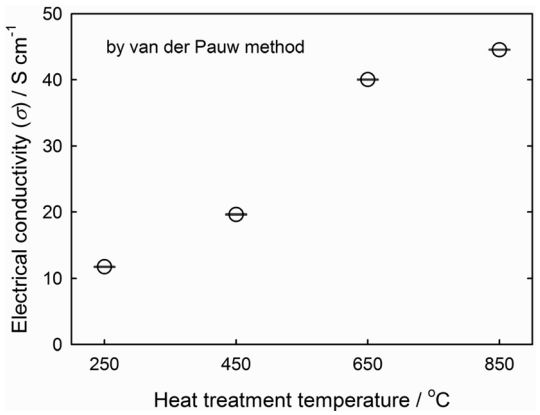

Fig. 3. Electrical conductivity of *e*-MCMBs obtained by the van der Pauw method.

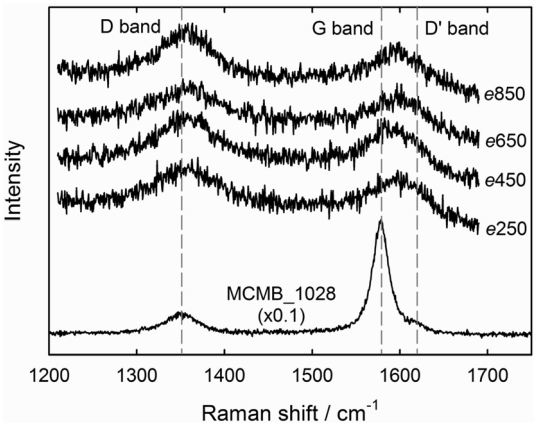

Fig. 4. Raman spectra obtained with *e*-MCMBs and MCMB_1028.

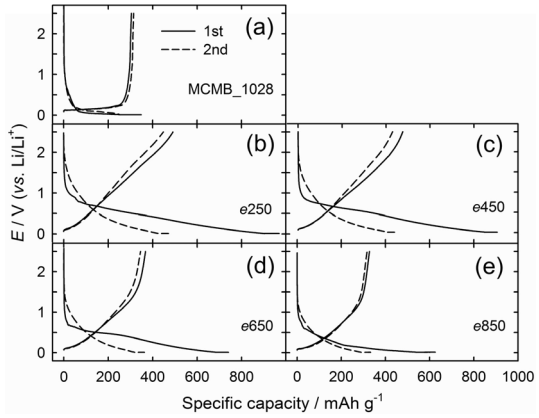

Fig. 5. The initial two charge-discharge voltage profiles obtained with Li/graphite cells: (a) MCMB_1028, (b) *e*250, (c) *e*450, (d) *e*650, and (e) *e*850. Charge/discharge rate = 0.2C. Cut-off range = 0.01~2.5 V (*vs.* Li/Li^+).

conductivity of *e*850 is, however, still smaller than that for MCMB_1028, reflecting that the removal of foreign atoms (restoration back to sp^2 carbons) is not completed. This feature is further ascertained from the Raman spectra (Fig. 4). The degree of graphitization (population of sp^2 carbons) can be estimated from the intensity ratio (I_D/I_G) of two Raman bands, where the *D* band is associated with structural disorders including sp^3 carbons and the *G* band from the vibration mode of $2E_{2g}$ along the sp^2 bonded (hexagonal) carbon layers. The intensity ratio is very small ($I_D/I_G \sim 0.15$) for MCMB_1028, indicative of a highly crystalline nature of the pristine graphite (negligible sp^3 carbons and foreign atoms). In contrast, the value for *e*-MCMBs is large ($I_D/I_G > 1$), reflecting a high degree of disorders and high population of foreign atoms.

3.2. Lithiation/de-lithiation mechanisms in expanded graphites

Fig. 5 represents the initial two charge-discharge voltage profiles obtained with the *e*-MCMBs and MCMB_1028 electrodes. Several features should be noted. First, the *e*-MCMB electrodes show a large irreversible capacity in the first cycle, such that the coulombic efficiency is ~50%. From the 2nd cycle, however, the coulombic efficiency becomes > 95%. This illustrates that the irreversible reactions take place mainly in the first cycle, which may be the electrolyte decomposition and concomitant SEI (solid electrolyte interphase) formation, and the Li trapping at the foreign atoms or in some defect sites.[18] Second, the de-lithiation capacity of *e*-MCMB electrodes is larger (for instance, ~500 mAh g^{-1} for *e*250) than that of the pristine counterpart (~330 mAh g^{-1} at 0.2C rate). This implies that the reversible Li storage sites are larger for the expanded graphites. The gradual decrease of de-lithiation capacity with an increase in heating temperature may, however, illustrate that the generation of such Li storage sites is more probable at lower temperatures. Third, the *e*-MCMB electrodes give a sloping charge/discharge voltage profile (more prominently, the charging profile), which is far different to the plateau-like profile observed with the pristine MCMB (Fig. 5(a)). It is known that Li^+ ions are intercalated/de-intercalated into/from the graphene layers of graphites in stepwise, giving rise to the plateau-like voltage profile. This is known as the stage phenomenon.[19] The monotonic sloping voltage profile for the *e*-MCMB electrodes manifest itself that the lithiation/de-lithiation mechanism prevailing in these electrodes is far different to the stage phenomenon. This difference is further confirmed from the *in-situ* dilatometry results shown in Fig. 6. As seen in Fig. 6(a), the pristine graphite (MCMB_1028) expands upon lithiation up to 10%, but contracts to the initial dimension upon de-lithiation. One apparent feature here is that the electrode is swollen and contracted in stepwise with several plateaus, which must be due to the stage phenomenon. In the case of the *e*250 electrode, however, the dilatometry profile is featureless and monotonic (Fig. 6(b)), strongly suggesting that the lithiation/de-lithiation mechanism is far different to the stage phenomenon.

Matsuo *et al.*[11] have proposed a bi-layer intercalation of Li^+ ions to account for the larger capacity observed with the partially reduced graphite oxides. Here, two-fold layers

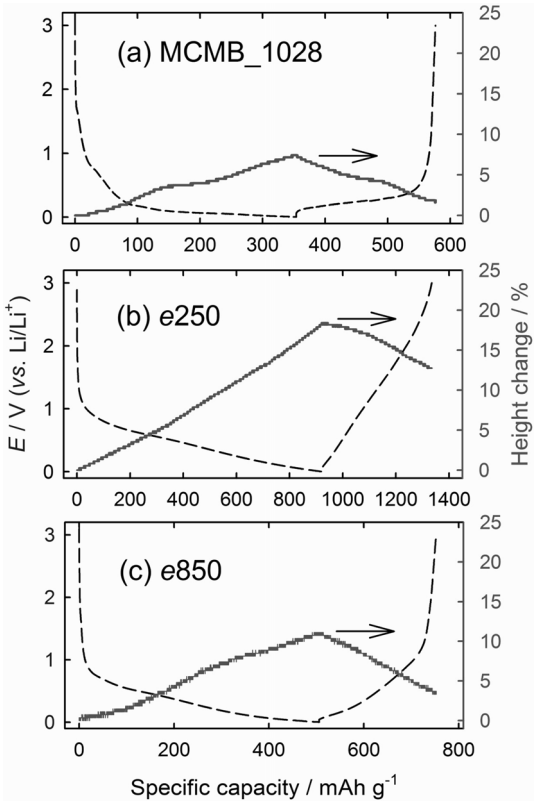

Fig. 6. *In-situ* dilatometry profiles obtained with three electrodes. The charge/discharge voltage profiles are overlapped. Charge/discharge rate = 0.2C. Cut-off range = 0.003~3 V (*vs.* Li/Li$^+$).

of Li$^+$ ions are assumed to be formed in each interlayer gap, in which oxygen or carbon atoms play as the Li$^+$ acceptor to stabilize the bi-layer structure. This bi-layer Li$^+$ intercalation mechanism seems to be plausible to explain the charge/discharge voltage profile observed with the *e*250 electrode (Fig. 5(b)) since the Li$^+$ uptake/removal takes place continuously (not stepwise). The dilatomerty profile shown in Fig. 6(b) may also be accounted for by this mechanism since the electrode height change of *e*250 is twice as large (~20%) as that of MCMB_1028. Note that Li$^+$ ions are intercalated as a single layer in each graphene layer in highly crystalline graphites by the stage phenomenon. Another difference in the dilatomerty profiles is that the swollen electrode, upon lithiation, does not restored to the original dimension in the *e*250 electrode, whereas the electrode expansion/contraction is reversible in the pristine graphite. The incomplete contraction observed with the *e*250 electrode may be explained by the Li trapping inside the interlayer gaps. Namely, the electrode is swollen with bi-layer intercalation of Li$^+$ ions, but is not fully contracted since the Li$^+$ ions remain inside the interlayer regions.

It is noted in Fig. 5 that the sloping voltage profiles become more plateau-like with an increase in the heat-treatment temperature. When the dilatometry profiles are compared for the *e*250 and *e*850 electrodes, the latter shows an intermediate behavior between the stepwise and monotonic change, suggesting that the lithiation/de-lithiation mechanism becomes closer to that of pristine graphite with an increase in the heat-treatment temperature. It is likely that the bi-layer Li$^+$ insertion mechanism prevails in the expanded graphites that are heat-treated at lower temperatures.

3.3. Rate capability of expanded graphites according to heat-treatment temperature

The cycle performance and rate capability of *e*-MCMB electrodes are presented in Fig. 7(a) and 7(b), respectively. In the initial few cycles, the *e*-MCMB electrodes deliver a higher capacity than the pristine one, but the values

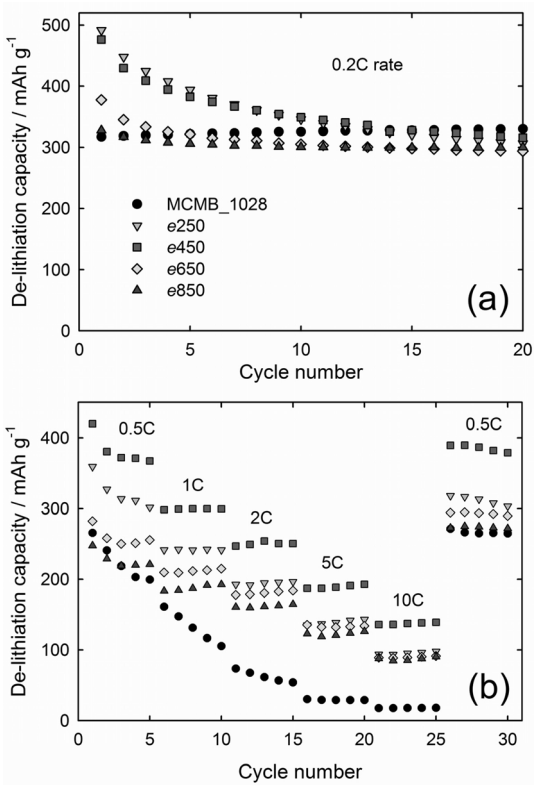

Fig. 7. (a) Cycle performances and (b) rate performances of *e*-MCMBs at 0.5~10C. Cut-off range = 0.01~2.5 V (*vs.* Li/Li$^+$).

become comparable to that for the pristine graphite due to a continuous capacity fading. The capacity fading in the *e*-MCMB electrodes may be attributed to the larger volume change than that for the pristine one, which may lead to a breakdown of the electrically conductive networks in the electrode layers.

As shown in Fig. 7(b), all the expanded graphite electrodes show a superior rate performance to the pristine one. The de-lithiation capacity of the latter electrode amounts to 280 mAh g^{-1} at 0.5C, but becomes 20 mAh g^{-1} at 10C. Many factors control the rate capability of graphitic carbons, for instance, the solid-state Li^+ ion diffusion through interlayer gaps and electrical conductivity. Of the two factors, the former seems to be dominating in controlling the rate capability of expanded graphites since the *e*-MCMBs exhibit a poorer electrical conductivity as compared to the pristine one. That is, the interlayer distance (d_{002}) is larger for the *e*-MCMBs, thereby a higher Li^+ ion diffusion can be assumed in these electrodes. When the rate capability is compared for the series of expanded graphite electrodes, the best rate performance is observed with *e*450 (Fig. 7(b)). The *e*450 electrode delivers a comparable de-lithiation capacity to that of *e*250 at a slower rate (0.2C) (Fig. 7(a)). At the higher rates (0.5~10C), however, a larger capacity is observed with *e*450 (Fig. 7(b)). As shown in Fig. 2(b), the interlayer distance becomes smaller with an increase the heat-treatment temperature, whereas the electric conductivity shows the opposite trend (Fig. 3). In the series of expanded graphites, *e*250 has the largest interlayer distance but carries the poorest electrical conductivity. The *e*850 electrode shows the highest conductivity but smallest interlayer gap. The best trade-off between the interlayer distance and electrical conductivity seems to be made with *e*450, giving rise to the best rate performance.

4. Conclusion

The expanded graphites (*e*-MCMBs) that differ in the interlayer distance and electrical conductivity are prepared by a heat-treatment of graphite oxide that in turn prepared by oxidizing a graphite powder (MCMB_1028) in highly acidic condition. The lithiation/de-lithiation mechanism involved in the expanded graphites is not the stage phenomenon that prevails in the highly crystalline graphites. With an increase in the heat-treatment temperature, the interlayer distance becomes smaller whereas the electrical conductivity increases. The *e*450 electrode shows the best rate performance among the series of expanded graphites, which is the result of a trade-off between the interlayer distance and electrical conductivity.

Acknowledgement

This work was supported by the WCU program through the National Research Foundation of Korea funded by the Ministry of Education, Science and Technology (R31-10013).

References

1. T.D. Tran, J.H. Feikert, R.W. Pekala and K. Kinoshita, *J. Appl. Electrochem.*, **26**, 1161 (1996).
2. S.S. Zhang, K. Xu and T.R. Jow, *J. Power Sources*, **160**, 1349 (2006).
3. M. Fujimoto, Y. Shouji, T. Nohma and K. Nishio, *Electrochemistry*, **65**, 949 (1997).
4. K. Zaghib, F. Brochu, A. Guerfi and K. Kinoshita, *J. Power Sources*, **103**, 140 (2001).
5. W.C. Choi, D. Byun, J.K. Lee and B.W. Cho, *Electrochim. Acta*, **50**, 523 (2004).
6. A. Nagai, K. Shimizu, M. Maeda and K. Gotoh, in *Lithium-Ion Batteries: Science and Technologies*, M. Yoshio, R.J. Brodd and A. Kozawa, Eds., Springer, New York (2009).
7. T.F. Fuller, M. Doyle and J. Newman, *J. Electrochem. Soc.*, **141**, 1 (1994).
8. M.W. Verbrugge and B.J. Koch, *J. Electrochem. Soc.*, **146**, 833 (1999).
9. E. Matuyama, *J. Phys. Chem.*, **58**, 215 (1954).
10. Y. Matsuo and Y. Sugie, *Electrochem. Solid State Lett.*, **1**, 204 (1998).
11. Y. Matsuo and Y. Sugie, *J. Electrochem. Soc.*, **146**, 2011 (1999).
12. S.B. Yang, H.H. Song and X.H. Chen, *Electrochem. Commun.*, **8**, 137 (2006).
13. W.S. Hummers and R.E. Offeman, *J. Am. Chem. Soc.*, **80**, 1339 (1958).
14. B.H. Ka and S.M. Oh, *J. Electrochem. Soc.*, **155**, A685 (2008).
15. L.J. van der Pauw, *Philips Technical Review*, **20**, 220 (1958).
16. T. Kim, S. Park and S.M. Oh, *J. Electrochem. Soc.*, **154**, A1112 (2007).
17. S. Park, T. Kim and S.M. Oh, *Electrochem. Solid State Lett.*, **10**, A142 (2007).
18. T. Zheng, J.S. Xue and J.R. Dahn, *Chem. Mater.*, **8**, 389 (1996).
19. M. Hahn, H. Buqa, P.W. Ruch, D. Goers, M.E. Spahr, J. Ufheil, P. Novak and R. Kotz, *Electrochem. Solid State Lett.*, **11**, A151 (2008).